Optics & Laser Technology 155 (2022) 108426

Contents lists available at ScienceDirect

Optics and Laser Technology

journal homepage: www.elsevier.com/locate/optlastec

Hybrid optical fiber Fabry-Perot interferometer for nano-displacement sensing

Monserrat Alonso-Murias [a,*], David Monzón-Hernández [a,*], Enrique Antonio-Lopez [b], Axel Schülzgen [b], Rodrigo Amezcua-Correa [b], Joel Villatoro [c,d]

[a] Centro de Investigaciones en Óptica A.C., Loma del Bosque 115, C.P. 37150 León, Gto., Mexico
[b] CREOL The College of Optics and Photonics, University of Central Florida, Orlando, 162700 FL, USA
[c] Department of Communications Engineering, University of the Basque Country UPV/EHU, Bilbao 48013, Spain
[d] IKERBASQUE-Basque Foundation for Science, Bilbao E-48011, Spain

ARTICLE INFO

Keywords:
Displacement sensing
Optical fiber sensors
Fiber optics
Fabry-Perot interferometer
Modal interferometer
Supermode interference
Multicore fibers

ABSTRACT

Nano-displacement sensing based on an extrinsic hybrid fiber Fabry-Perot interferometer is proposed and demonstrated. The lead-in fiber tip of such an interferometer consists of a strongly-coupled multicore fiber section fusion spliced to a single-mode fiber. The referred lead-in fiber tip is placed in front of a microscope slide, whose rear surface is coated with a high reflecting layer. The gap between the end-face of the fiber tip and the layer is composed of an air cavity in series with a glass one. Light exiting from the lead-in fiber tip is partially reflected at the fiber-air and air-glass interfaces and the reflecting layer generating three beams that are recoupled into the multicore fiber and combined with supermode interference. By making the optical path length of the air cavity slightly different from the glass one, it is possible to generate an envelope in the interference spectra with a larger period. Thus, by tracking the shift of such an envelope, displacements of 0.47 nm can be resolved. The nano-displacement sensing approach reported here is easy to implement; moreover, the sensitivity, resolution, and dynamic range can be reconfigured by an appropriate selection of the glass cavity.

1. Introduction

Nanotechnology is a multidisciplinary field of knowledge that deals with understanding, modeling, controlling, and manipulating the matter at a portion ranging from 1 to 100 nm [1]. The strong influence of nanotechnology in science and technology has modeled and defined almost every aspect of modern life. At the nanometer scale, the selection of an appropriate measurement method may be a complicated task. For example, displacement measurements with sub-nanometer accuracy can be challenging with most of electrical and mechanical sensors due to their low resolution. For such cases, the high sensitivity of optical phenomenon associated with laser feedback interferometry [2], optical encoder [3], and grating interferometric cavity [4] have been revealed as the most suitable alternatives since they allow non-contact displacement measurement with high resolution even at a sub-nanometer level. However, these schemes are not an option for measuring in hard-to-reach areas, as their performance requires several items, bulky optical components, and controlled environments that may complicate their implementation.

Optical fiber interferometers are intrinsically compact and flexible devices with no moving parts, which make them ideal for distance measurements in reduced spaces. Additionally, they combine high sensitivity, resolution, and long dynamic range [5]. Among the different fiber interferometers proposed so far, the extrinsic fiber Fabry-Perot is appealing since it enables the development of no-contact displacement sensors with nanometer resolution [6]. Moreover, it can be configured to measure other physical magnitudes such as pressure [7,8], temperature [9], strain [10], vibration [11,12] magnetic field [13], or liquid level [14].

Displacement of a target can be measured with an extrinsic Fabry-Perot interferometer by analyzing the shift of the interference pattern generated by multiple reflected beams [15,16]. In this case, the applied demodulation method is influential given that it determines the performance of the displacement sensor. The advantage of monitoring the shift of an interference pattern includes immunity to intensity fluctuations of the light source. However, for nanometer-resolution displacement measurements, intensity-modulated interrogation methods [17] are preferable since minute wavelength shifts of the interference pattern

* Corresponding authors.
E-mail address: dmonzon@cio.mx (D. Monzón-Hernández).

https://doi.org/10.1016/j.optlastec.2022.108426
Received 19 January 2022; Received in revised form 21 May 2022; Accepted 28 June 2022
Available online 4 July 2022

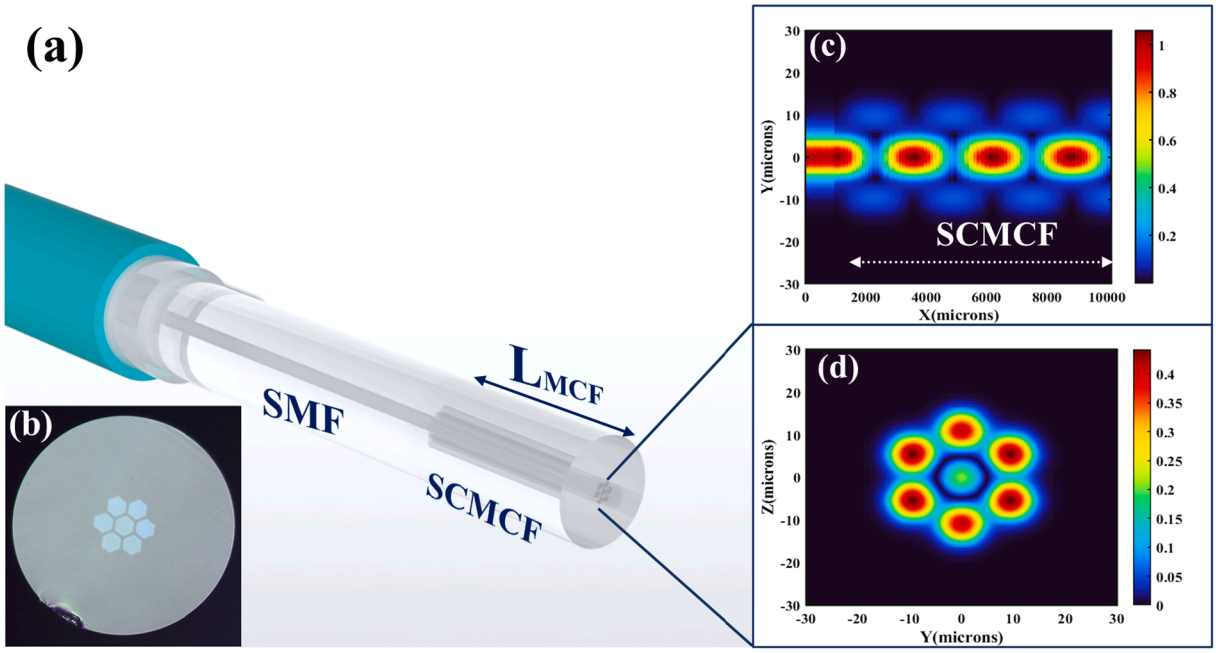

Fig. 1. (a) Sketch of a supermode interferometer in reflection scheme. (b) Micrograph of a strongly-coupled multicore fiber of seven cores. Simulation of the SMF-SCMCF structure with L_{MCF} = 9.2 mm: (c) light propagation in the transverse section and (d) mode distribution on the end-face.

may be complicated to detect with conventional spectrometers. Thus, it is desirable to have an interference pattern with large free spectral range (FSR), which means that the cavity length of the interferometer must be small. Albeit, the Fourier domain analysis is one of the most common and reliable methods to analyze the reflectance of a single or multiple cavities, it offers low resolution, and hence it is not suitable for nanometric displacements [18].

In recent years, it has been demonstrated that the sensitivity and resolution of fiber interferometers can be enhanced by taking advantage of the optical analog of the Vernier effect [19–23]. Such an effect is achieved when the period of the interference patterns of the sensing interferometer and the auxiliary or reference interferometer, arranged either in series [24,25] or in parallel [26–28], are very similar. In the Vernier effect, the multiplication or sum of two interference patterns produce a modulation envelope with large FSR. By monitoring such an envelope, higher sensitivities can be achieved. Recently, some displacement sensors based on the Vernier effect have been reported [29–31]. Fabry-Perot interferometric displacement sensors composed of two cavities in series that achieve nanometer resolution have been proposed and demonstrated as well [30,31]. Although the displacement sensors reported in [29–31] have good performance, their fabrication or implementation tend to be complex, which may be impractical in many applications.

In this work, we propose and demonstrate a nanometer displacement sensor based on a hybrid supermode-Fabry-Perot interferometer. The lead-in fiber tip consists of a millimeter-long segment of coupled-core optical fiber fusion spliced to a conventional single mode fiber. The external element (target) of the sensor is a microscope slide, which was placed in front of the lead-in fiber tip. A glass cavity and an air cavity with millimeter size compose the hybrid interferometer. At each interface of the cavities, the light is reflected, thus, the interference of three beams is combined with the supermode interference in the multicore fiber. Thus, the reflected spectrum exhibited a pattern produced by the interference of supermodes and the multiple-beam interference of the cavities. The lead-in fiber tip was moved until the optical path lengths of the air and glass cavity were almost equal. At this position, a characteristic modulation envelope arose in the resulting interference pattern. A nanometric displacement of the lead-in fiber tip induced a change in the air cavity length and resulted in a wavelength shift of the envelope. Such a shift was quantified for various displacements, thus obtaining a resolution of 0.47 nm. The implementation of the hybrid interferometer is straightforward, it does not require a costly and complex fabrication process, and its scheme can be reconfigured enabling to adjust it for different applications. The sensitivity, resolution, and dynamic ranges can also be adjusted.

2. Design, fabrication and operating principle of the extrinsic hybrid fiber Fabry-Perot interferometer

2.1. Supermode interferometer: lead-in/out fiber tip

In this work, we focus on a supermode interferometer based on single-mode fiber (SMF) and a section of strongly coupled multicore fiber (SCMCF), as shown in Fig. 1(a), for displacement measurement at a nanometer scale. The supermode interferometer as a lead-in/out element has not yet been addressed widely in the sensing field. So far, the use of the end-face of a supermode interferometer has been used mainly for refractive index measurements based on the Fresnel reflection [32,33].

In the design and fabrication of the lead-in/out fiber tip, the cross-section and the length of the SCMCF are parameters to be considered. Regarding the former, the SCMCF used in this work, comprises seven identical cores, each with a diameter of 9 μm. Such cores are distributed in a hexagonal shape around a central core, the separation between cores is 13 μm. A micrograph of the cross section of the SCMCF is shown in Fig. 1(b). In this structure, the interference takes place due to the beating between two supermodes [34–36], which can be viewed as a periodic energy transfer from the central core to neighbor cores (as displayed in Fig. 1(c)). The distance at which it occurs is known as coupling length (L_c), defined by

$$L_c = \pi/(|\beta_2 - \beta_1|) \quad (1)$$

where β_1 and β_2 are the propagation constants of the two interfering supermodes. Therefore, the performance of the lead-in/out fiber tip depends on the SCMCF length (L_{MCF}) as demonstrated in Ref. [37]. In the supermode interferometer, a multiple of the coupling length gives either

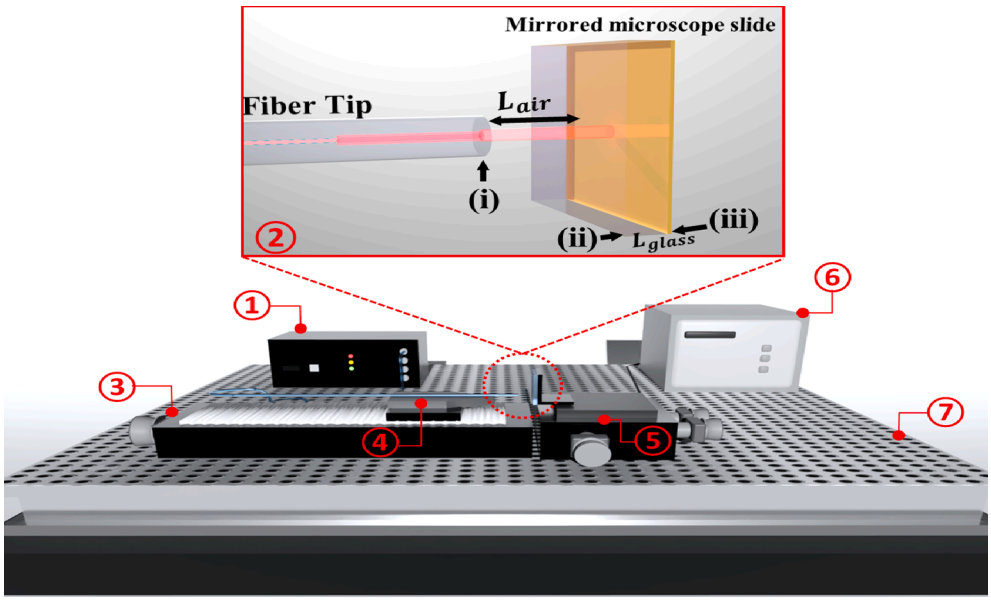

Fig. 2. Experimental set-up: 1. FBG interrogator, 2. extrinsic hybrid fiber Fabry-Perot interferometer, 3. motorized translation stage (1-axis), 4. V-groove holder, 5. motorized translation stage (3-axis), 6. stepper motor controller, 7. Optical table.

constructive or destructive interference in the central core of the SCMCF. Constructive interference is visualized when most of the energy is distributed in the central core of the SCMCF, and it is achieved when

$$L_{MCF} = mL_c (2)$$

where m is an integer. Although the constructive interference is exploited in the interferometric sensors, here this condition will make that lead-in fiber tip works similar to a single-mode fiber; i.e., the exit beam will be more diffracted at a short distance. In this sense, the supermode interference must be exploited in a lead-in fiber tip when destructive interference occurs. It can be viewed as most of the energy is distributed in the cores around the central core of the SCMCF as displayed in Fig. 1(d). So, the output light will emerge from a larger area. This condition is accomplished when

$$L_{MCF} = (2m+1)L_c/2 (3)$$

Thus, the length of the segment of the multicore fiber was calculated according to Eq. (3). The fabrication process of the SMF-SCMCF structure is simple and requires only a few steps. Firstly, the SMF was fusion spliced to the SCMCF utilizing the default fusion splicing program of a Fujikura FSM-100P splicer. Then, the multicore fiber was cleaved to length of 9.2 mm. In Ref. [37], the above-mentioned conditions of constructive and destructive interference were analyzed with more detail. The optimal length of the SCMCF was 9.2 mm to ensure a wider distribution of light in the seven cores at the fiber tip end-face. Thus, the light exiting the SCMCF tip is broader, so it can propagate longer distances and be recoupled by the same SCMCF. This supermode interferometer was used to demonstrate an EFFPI with enhanced visibility that allowed to measure displacements as long as 50 mm [37].

2.2. The extrinsic hybrid fiber Fabry-Perot interferometer

The extrinsic fiber Fabry-Perot interferometer has been successfully proposed to measure the distance between the optical fiber tip end-face and a reflecting parallel surface placed in front. The gap between the surfaces is known as cavity, when the gap contains two or more materials (for example air and glass) the cavity is referred as hybrid. In this work, an extrinsic hybrid fiber Fabry-Perot interferometer (E-HFFPI) is proposed to measure displacement with nanometer resolution. The light beam exiting from the fiber tip is actually propagated through an air gap and a piece of glass as it can be seen in element 2 of Fig. 2. In the structure of the E-HFFPI shown in Fig. 2 the label (i) indicates the end-face of the lead-in SCMCF tip, (ii) the front surface of the microscope slide, and (iii) the highly reflective layer (mirror) deposited over the rear surface of the microscope slide, each one with a reflectivity of R_1, R_2, and R_3 respectively. Light propagating in the lead-in fiber tip is partially reflected at the interface (i), the transmitted light is partially reflected at the interfaces (ii) and (iii), and then are recoupled at the multicore fiber where they interfere among them and with the beam reflected at the interface (i). The mathematical expression to describe the intensity reflected of an E-HFFPI, considering a single-mode fiber tip, can be described by the following relation:

$$I_{E-HFFPI} = \Big\{R_1 + R_2(1-R_1)^2\eta_1 + R_3(1-R_1)^2(1-R_2)^2\eta_2 + 2\sqrt{R_1R_2\eta_1}\,(1-R_1)cos[2\pi/\lambda^*(2\mathrm{OPL_{air}})] + 2(1-R_1)(1-R_2)\sqrt{R_1R_3\eta_2}\,cos\big[2\pi/\lambda^*\big(2\mathrm{OPL_{air}} + 2\mathrm{OPL_{glass}}\big)\big] + 2(1-R_1)^2(1-R_2)\sqrt{R_2R_3\eta_1\eta_2}\cos\big[2\pi/\lambda^*\big(2\mathrm{OPL_{glass}}\big)\big]\Big\}I_0 (4)$$

where λ is the wavelength of the light, η_1 and η_2 are the coupling coefficient of the beam reflected at the surface (ii) and (iii), respectively. The optical path lengths (OPL) of the interference terms are described by $OPL_{air} = n_{air} \bullet L_{air}$, $OPL_{glass} = n_{glass} \bullet L_{glass}$, and

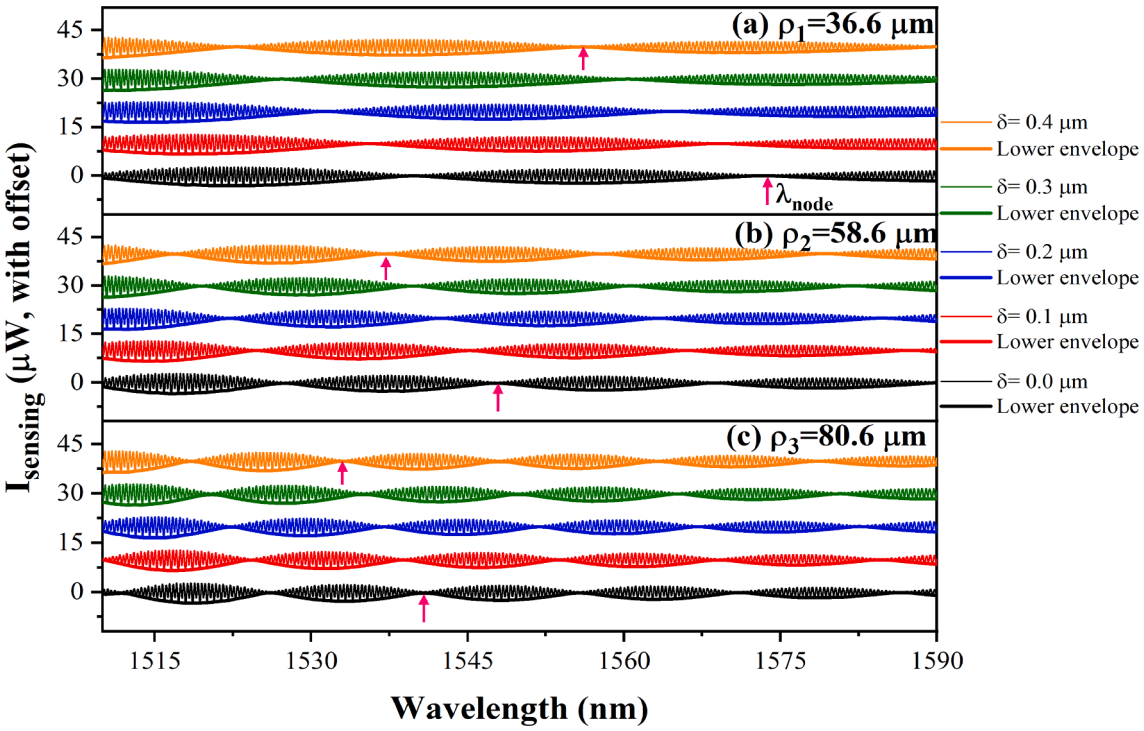

Fig. 3. Simulated spectra of $I_{sensing}$, highlighting the lower envelope, when the fiber tip position was decreased by $\hat{I} = = 0.1$ μm, the difference of the OPL s is (a) $\rho_1 = 36.6$ μm (b) $\rho_2 = 58.6$ μm, and (c) $\rho_3 = 80.6$ μm.

$OPL_{air+glass} = n_{air} \bullet L_{air} + n_{glass} \bullet L_{glass}$ for glass, air, and total cavity; respectively. I_0 is the intensity of the light incident in the fiber tip end-face.

In this E-HFFPI, the displacement of the fiber tip modifies the OPL_{air} since OPL_{glass} is constant, however, due to the complex interference spectra produced by the superposition of three interference terms (Eq. (4)), tracking the wavelength displacement of a maximum or a minimum of the interference pattern can be a difficult task. The spectra of the reflected intensity are simpler when OPL_{glass} and OPL_{air} are equal, when this condition is achieved the reflected intensity is now described by,

$$I_{REF} = \Big\{R_1 + R_2(1-R_1)^2\eta_1 + R_3(1-R_1)^2(1-R_2)^2\eta_2 + 2\sqrt{R_1R_2\eta_1}\,(1 - R_1)cos\big[2\pi/\lambda^*\big(2\mathrm{OPL}_{\mathrm{glass}}\big)\big] + 2(1-R_1)(1-R_2)\sqrt{R_1R_3\eta_2}\,cos\big[2\pi/\lambda^*\big(4\mathrm{OPL}_{\mathrm{glass}}\big)\big] + 2(1-R_1)^2(1-R_2)\sqrt{R_2R_3\eta_1\eta_2}\,cos\big[2\pi/\lambda^*\big(2\mathrm{OPL}_{\mathrm{glass}}\big)\big]\Big\}I_0 \quad (5)$$

By overlapping the interference pattern of an E-HFFPI, where the reference and sensing cavities are connected either in series or in parallel [25,38], it will give place to modulation of the interference pattern with an envelope function formed on it. Here, the glass cavity is considered as a reference cavity with a constant *OPL*. Meanwhile, the air cavity can be used for nano-displacement measurements. Small changes in $OPL_{air} = OPL_{glass} + \rho$, where $\rho \ll OPL_{glass}$, could produce a small displacement of the modulated intensity that can be expressed as,

In order to highlight the changes of the envelope produced in the reflected intensity of Eq. (5) by the increment ρ in the *OPL* of air cavity, it is necessary to compare the spectrum of I_{REF} with I_{SMF}. Subtraction of Eq. (5) from Eq. (6) results in the following expression

$$\begin{aligned} I_{sensing} &= I_{SMF} - I_{REF} \\ &= \Big\{2(1-R_1)\sqrt{R_1R_2\eta_1}\Big\{cos\big[4\pi/\lambda^*\big(OPL_{glass}+\rho\big)\big] - cos\Big[4\pi/\lambda^*\big(OPL_{glass}\big)\Big]\Big\} + 2(1-R_1)(1 - R_2)\sqrt{R_1R_3\eta_2}\Big\{cos\big[8\pi/\lambda^*\big(OPL_{glass}+\rho/2\big)\big] - cos\Big[8\pi/\lambda^*\big(OPL_{glass}\big)\Big]\Big\}\Big\}I_0 \quad (7) \end{aligned}$$

$$I_{SMF} = \Big\{R_1 + R_2(1-R_1)^2\eta_1 + R_3(1-R_1)^2(1-R_2)^2\eta_2 + 2\sqrt{R_1R_2\eta_1}\,(1-R_1)cos\big[2\pi/\lambda^*\big(2\mathrm{OPL}_{\mathrm{glass}}+2\rho\big)\big] + 2(1-R_1)(1-R_2)\sqrt{R_1R_3\eta_2}\,cos\big[2\pi/\lambda^*\big(4\mathrm{OPL}_{\mathrm{glass}} + 2\rho\big)\big] + 2(1-R_1)^2(1-R_2)\sqrt{R_2R_3\eta_1\eta_2}\,cos\big[2\pi/\lambda^*\big(2\mathrm{OPL}_{\mathrm{glass}}\big)\big]\Big\}I_0 \quad (6)$$

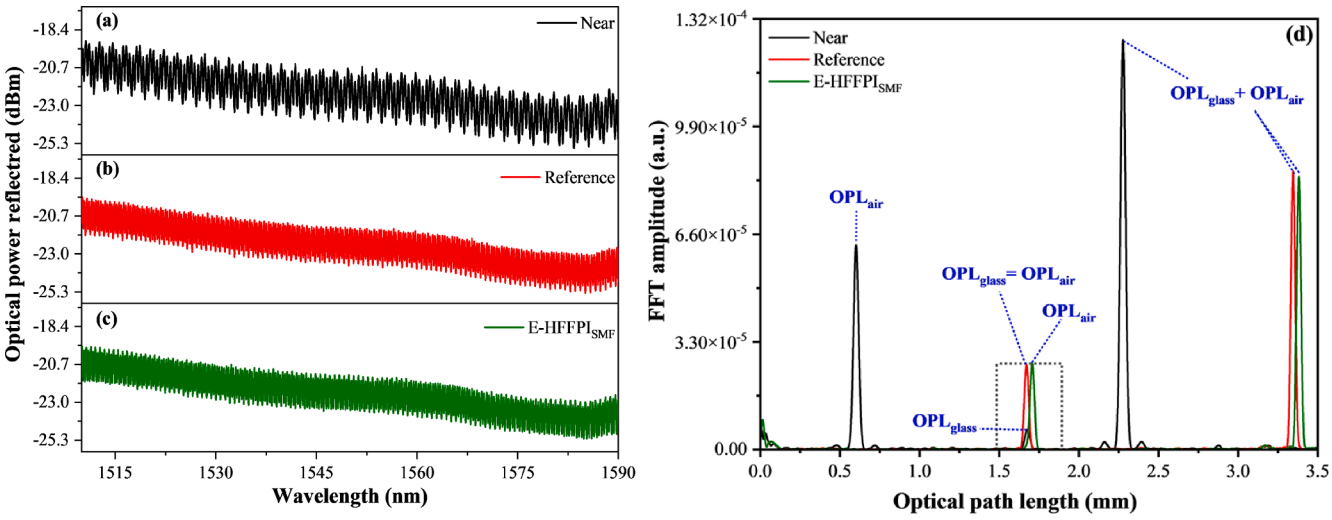

Fig. 4. Reflection spectrum of the E-HFFPI$_{SMF}$ when (a) OPL$_{air}$ was smaller than OPL$_{glass}$, (b) when OPL$_{air}$ and OPL$_{glass}$ are equals, and (c) when OPL$_{air}$ was equal to 1.70729 mm. (d) The corresponding Fourier spectra of the reflection spectra shown in (a)-(c).

This expression was used to analyze the response of the E-HFFPI for three different initial values of ρ and at each position several nano displacements (δ) of the optical fiber tip respect to the surface of the piece of glass were performed. Fig. 3(a) shows the simulated spectra when ρ_1 = 36.6 μm andOPL_{glass} = 1668.82 μm, then $OPL_{air} = OPL_{glass} + \rho_1$ = 1705.42 μm, and for displacements of δ = 0, 0.1, 0.2, 0.3, and 0.4 μm. The spectra unfold a dense fringe pattern modulated by two envelopes; denoted here as above and below. From Fig. 3(a), it can be appreciated that the envelope has a larger FSR than the interference fringes. The lower envelope is highlighted in each spectrum of Fig. 3(a), the pink arrows are used to indicate the initial and final position of a node. In the figure, it can be clearly seen that a decrement in the air cavity length from the initial position 1705.42 μm, when ρ_1 = 36.6 μm, produces a blue-shift of the node. For the other two cases, when ρ_2 = 58.6 μm and ρ_3 = 80.6 μm, the simulated spectra and their lower envelopes are shown in Fig. 3(b) and (c), respectively. A similar blue-shift is appreciated in the three cases for ρ_1, ρ_2, and ρ_3 when air cavity was decreased from 0 to 400 nm in steps of 100 nm. The shift of the envelope is smaller for larger values of the initial position: ρ_1. It is also important to note that the FSR of the envelopes decreases for larger values of ρ, given that the FSR of the sensing cavity interference pattern decreases, see Fig. 3(a)–(c). By assuming that the wavelength shift of one envelope node can be determined with a resolution of 0.1 nm, the expected displacement resolution of the scheme proposed here is around 1 nm.

3. Experimental results

3.1. Performance of the E-HFFPI build with an SMF

In order to validate the above predictions, a series of experiments were carried out. Since the analysis of the extrinsic Fabry-Perot was done by considering an SMF (E-HFFPI$_{SMF}$) as a lead-in and- out fiber tip, we tested first an interferometer constructed with an SMF. A representation of the experimental set-up used is shown in Fig. 2. The SMF was attached to a V-groove holder that was placed on a motorized translation stage (NRT150/M, Thorlabs). The mirrored microscope slide from Sigma-Aldrich (thickness = L_{glass} ≈ 1100 μm, refractive index = n_{glass} = 1.507 at 1550 nm) was placed on top of the XYZ motorized translation stage (NanoMax300, Thorlabs) with 50 nm resolution. The motorized translation stages were connected to a stepper motor controller (BSC203, Thorlabs). The SMF was connected to a fiber Bragg grating interrogator (sm125, MicronOptics) to collect the reflection spectra.

Firstly, the SMF tip was approached to the surface of the glass slide; i. e., at a position far from meeting the Vernier effect, and the obtained

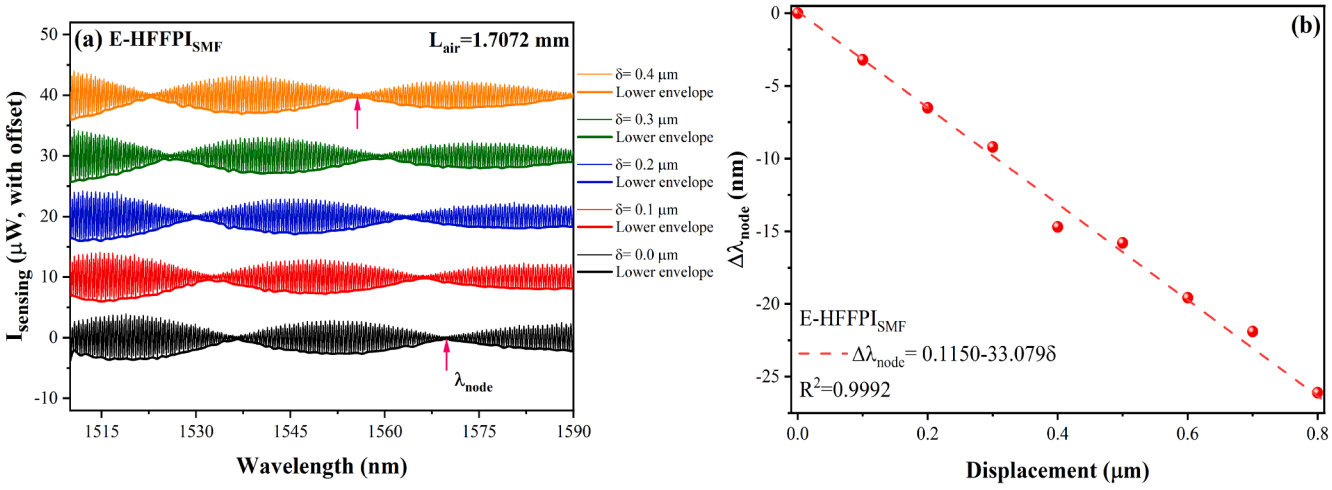

Fig. 5. (a) The calculated $I_{sensing}$ spectra and the lower envelope obtained for displacements of 0.1 μm with the initial L_{air} equal to 1.7072 mm. (b) Wavelength shift of the selected node to construct the characteristic curve of the $I_{sensing}$, evaluated to displacement of 0.1 μm.

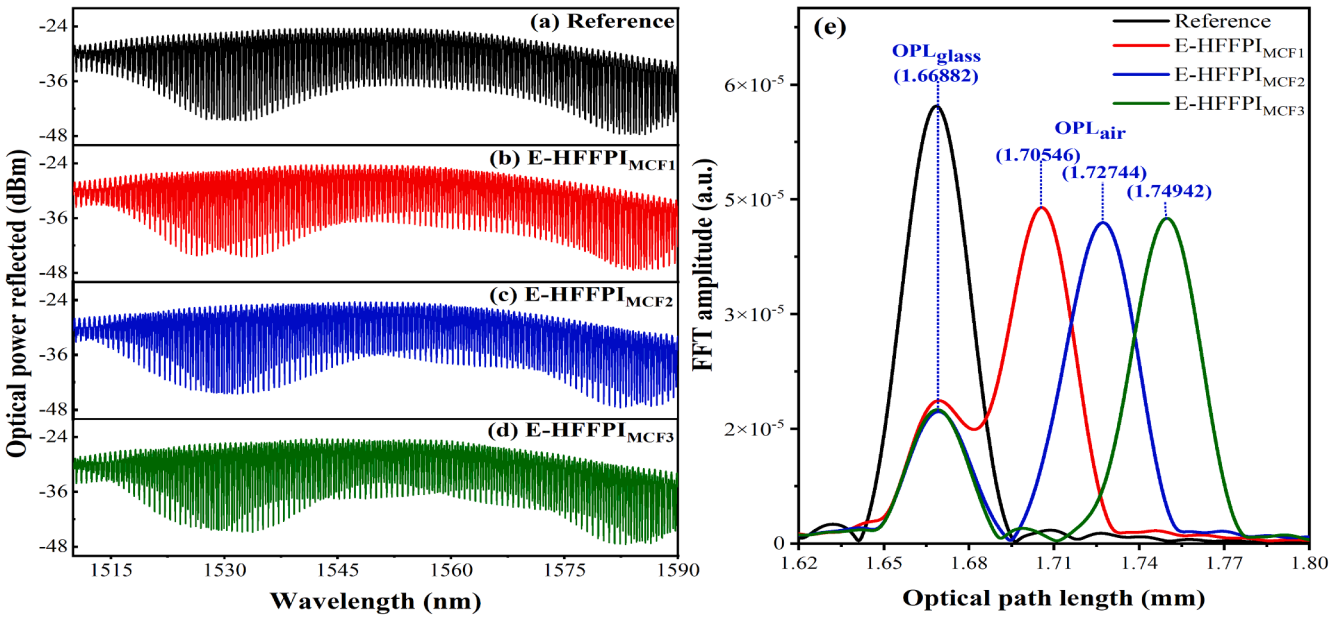

Fig. 6. (a) Reference spectrum of the E-HFFPI$_{MCF}$ when OPL$_{air}$ and OPL$_{glass}$ are equal. (b)-(d) Reflection spectrum for the three E-HFFPI$_{MCF}$s with different L$_{air}$. (c) FFT amplitude results corresponding to (a)–(d).

reflected spectrum, shown in Fig. 4(a), was recorded as the near signal $I_{E\text{-}HFFPI}$. The fast Fourier transform (FFT) algorithm reported in [39] was used to calculate the Fourier transform of the optical spectrum shown in Fig. 4(a), such a Fourier spectrum is shown in the black line graph of Fig. 4(d). In this Fourier spectrum, three peaks sufficiently spaced are appreciated. The first peak indicates the OPL of air cavity, the second peak, that is shown within the dashed line rectangle, indicates the OPL of glass cavity, and the third one indicates the sum of the OPL of air and glass cavity. The amplitude of the OPL$_{glass}$ peak, as compared to the OPL$_{air}$ peak, is very small, which is due to the low visibility of the fringe pattern caused by the large intensity difference of the two interfering beams, one is reflected at the air-glass interface ($R_2 \approx 4\%$) and the other one at the mirror deposited at the rear surface of the glass slide ($R_3 \approx 90\%$). Then, the fiber tip was carefully adjusted until the *OPL$_{air}$* was equal to *OPL$_{glass}$*. The obtained reflection spectrum was recorded as the reference signal I_{REF}, as shown in Fig. 4(b). Its FFT spectrum was calculated and shown in the red graph of Fig. 4(d). Only two peaks were observed since the peaks produced by the air cavity and glass cavity are overlapped (see the dashed line rectangle in the figure). Later, the SMF tip was displaced 36.6 μm away from the glass surface, the reflection spectrum of the I_{SMF} is depicted in Fig. 4(c). The reflection spectra shown in Fig. 4(a)–(c) exhibit a pattern with visibility smaller than 1 dB, but it

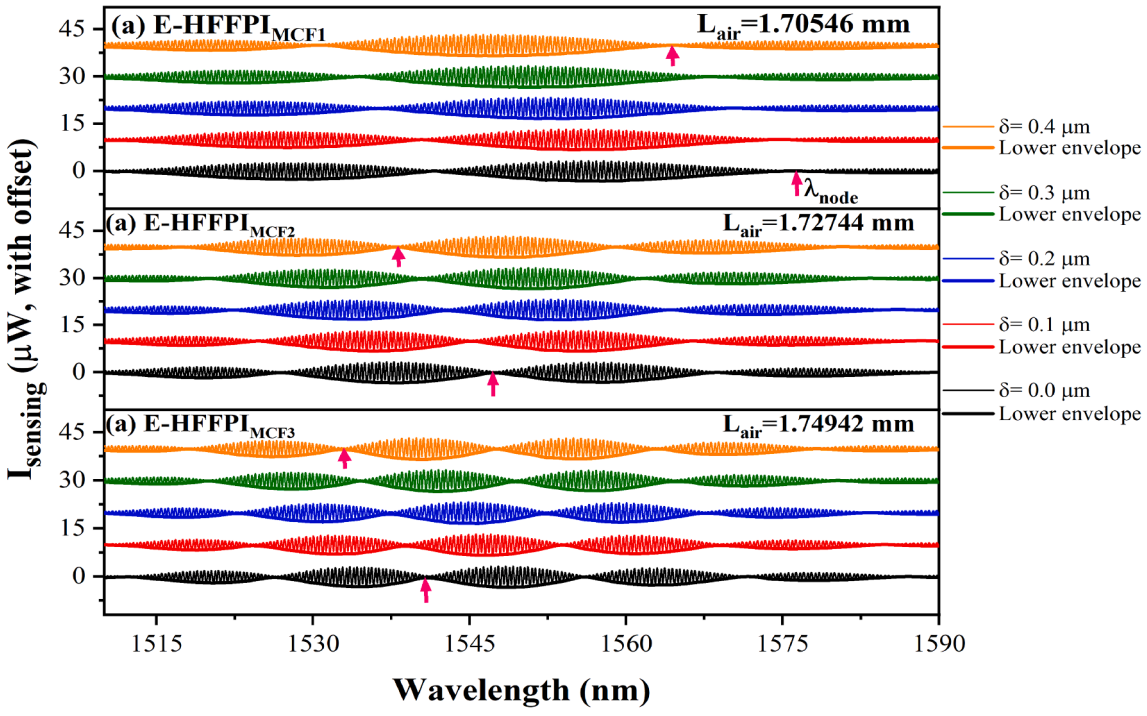

Fig. 7. The $I_{sensing}$ spectra obtained when the reference spectrum is subtracted from the reflection spectrum, and its lower envelope to displacements of 0.1 μm for an E-HFFPI$_{MCF}$ with L$_{air}$ equal to (a) 1.70546 mm, (b) 1.72744 mm and (c) 1.74942 mm.

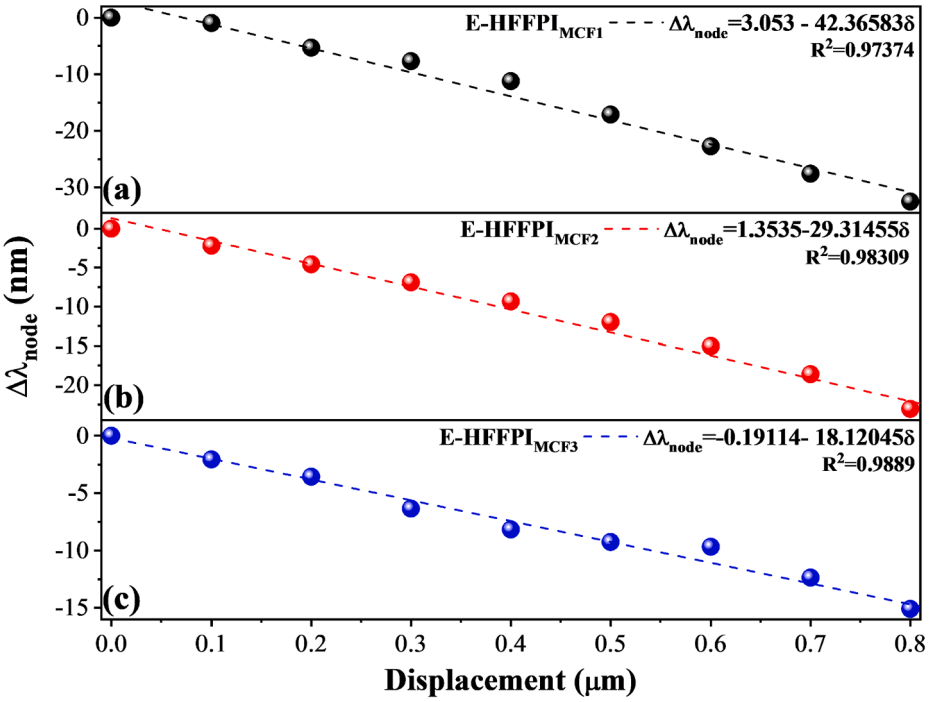

Fig. 8. Wavelength shift of one of the nodes of the lower envelope as a function of the displacements of 0.1 μm for the (a) E-HFFPI$_{MCF1}$, (b) E-HFFPI$_{MCF2}$, and (c) E-HFFPI$_{MCF3}$.

is possible to distinguish slight differences among the spectra of Fig. 4(b) and (c). Accordingly, in the Fourier domain, instead of three, two peaks were observed, see the green graph of Fig. 4(c). For this case, it is impossible to observe the peak corresponding to the OPL_{glass} mainly due to the low intensity of the beams recoupled to the core of the SMF at this distance. This is so because the light that exits from the SMF core broadens rapidly. The absence of the peak in Fourier domain, associated with the glass cavity, made impossible to determine in this case the exact position of the OPL of glass cavity; though, this one can be known from the spectrum obtained when fiber tip is close to the glass slide. But, in order to simplify the procedure, it is possible to assume that the reference position, when $OPL_{air} = OPL_{glass}$, is the one that produces the spectrum shown in Fig. 4(b).

After the preliminary calibration process, to stablish the initial position of the SMF tip where $L_{air} = OPL_{glass} \pm \rho$ that produces the spectrum shown in Fig. 4(c), the assessment of nano-displacement sensing was started by moving the mirrored glass slide towards the SMF tip in steps (δ) of 0.1 μm. At each position the reflected spectrum was recorded, and then it was subtracted by the reference spectrum in linear scale. The resulted spectra ($I_{sensing}$) are displayed in Fig. 5(a) where the envelopes obtained by the interpolation of the dips are also included. It can be seen that the FSRs of the envelopes are much larger than the interference fringes. In this regard, to quantify the displacement sensitivity of $I_{sensing}$, one of the nodes of the modulated interference patterns, i.e., a maximum of the lower envelope (λ_{node}) was tracked and correlated with the glass slide displacement. The selected node is indicated by a pink arrow in the initial (black line) and final (orange line) spectra of Fig. 5(a). The node shifted toward shorter wavelengths at each glass slide displacement because the air cavity length decreased. The tracked node wavelength shift ($\Delta\lambda_{node}$) and the adjusted linear fit are plotted in Fig. 5(b). From this curve, it was possible to estimate that $I_{sensing}$ has a displacement sensitivity of –33.07 nm/μm. While the $I_{sensing}$'s resolution was calculated to be equal to 0.60 nm, assuming a FBG interrogator resolution of 20 pm.

3.2. Performance of the E-HFFPI build with SCMCF

The procedure and the signal processing presented in Section 2.2 to decode the changes in the reflected intensity spectrum produced by the mirrored glass displacement can be achieved using an SMF. However, the impossibility to observe the peak in the Fourier spectrum (green plot of Fig. 4(d)) associated to the glass cavity seriously affected the performance of this approach. To overcome such limitations, it is proposed to construct an extrinsic Fabry-Perot (E-HFFPI$_{MCF}$) by splicing a section of SCMCF of 9.2 mm length to the SMF, the SCMCF acts as a lead-in/out fiber tip. The SCMCF tip was placed in the experimental set-up represented in Fig. 2. In order to analyze the effect of the initial OPL_{air} conditions, i.e., when $OPL_{air} = OPL_{glass} \pm \rho$ where $\rho \ll OPL_{glass}$, three experiments were made by using three different initial positions. The interferometers were labeled as E-HFFPI$_{MCF1}$, E-HFFPI$_{MCF2}$, and E-HFFPI$_{MCF3}$ and for each case ρ was equal to 36.6, 58.6, and 80.6 μm, respectively. The response of these interferometers was evaluated to displacements of 0.1 μm, following the same procedure used to evaluate the E-HFFPI$_{SMF}$ presented in Section 3.1. Firstly, the supermode interferometer was secured in a V-groove holder attached to a motorized translation stage. Then, the fiber tip position was adjusted to equal OPL_{air} and OPL_{glass}, the reflection spectrum obtained is shown in Fig. 6 (a); it was recorded and used as reference spectrum. After that, the fiber tip was moved a distance ρ away from the surface of the glass slide; the spectra for a ρ of 36.6 (E-HFFPI$_{MCF1}$), 58.6 (E-HFFPI$_{MCF2}$), and 80.6 μm (E-HFFPI$_{MCF3}$) are shown in Fig. 6(b)–(d), respectively. Importantly, the interference spectrum resulted in each case is the superposition of the supermode interference and the multiple beams interference of the extrinsic fiber Fabry-Perot interferometer [37]. The latter produces a large number of fringes in the E-HFFPI$_{MCF}$'s interference pattern. It is important to notice that a modulation with lobes appears underneath the spectrum and its number augments as ρ increases.

The FFTs of the reference spectrum and the reflected spectra of each E-HFFPI$_{MCF}$ shown in Fig. 6(a)–(d) were calculated and the resulted spectra are shown in Fig. 6(e). The position of the FFT peaks corresponds to the *OPLs* of the glass cavity and air cavity. For the reference spectrum (black), a single peak appears because the peaks are overlapped at 1.668

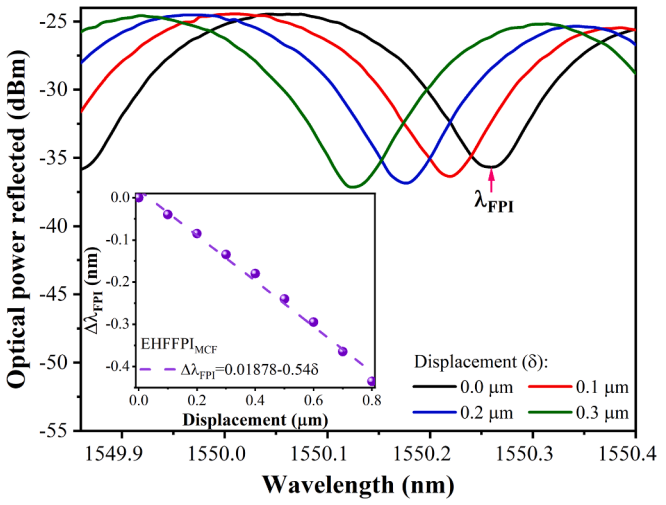

Fig. 9. A narrow region of the reflection spectrum of the E-HFFPI$_{MCF_2}$ to the measured displacement of 0.1 μm. Inset: Relation between wavelength of a minimum in the interference pattern, and the displacement.

mm. Unlike E-HFFPI$_{SMF}$, two separate peaks are observed in the FFT spectra of the E-HFFPI$_{MCF1}$ (red), E-HFFPI$_{MCF2}$ (blue), and E-HFFPI$_{MCF3}$ (green). The higher visibility of the interference pattern is due to the broader (less divergent) beam that emerges from the SCMCF as well as the larger area of the multicore fiber that is available for coupling the beams reflected from the two cavities.

As it was done with the E-HFFPI$_{SMF}$, the three E-HFFPI$_{MCF}$s were assessed for nano displacements sensing. The nano displacements were carried out by moving the mirrored glass slide towards the end-face of the supermodal interferometer tip in steps of 0.1 μm with a translation stage. The reflected spectra were recorded, and the reference spectrum was subtracted later in the linear scale from these spectra. The outcomes are the $I_{sensing}$ spectra for the E-HFFPI$_{MCF1}$, E-HFFPI$_{MCF2}$ and E-HFFPI$_{MCF3}$, shown in Fig. 7(a)–(c), respectively, where the lower envelopes are included.

In Fig. 7, it can appreciate that the FSRs of the lower envelopes are larger than the interference fringes. Also, the FSRs are different for each of the E-HFFPI$_{MCF}$s as it was predicted by the simulations (see Fig. 3). It implies that the sensitivity and resolution of the E-HFFPI$_{MCF}$s depend on the initial length, i.e., the optical length difference between the air and glass cavities. Accordingly, the wavelength of one of the nodes of the modulated interference patterns (λ_{node}) was tracked and correlated with the glass displacement for quantifying the performance of the E-HFFPI$_{MCF}$s. The shift of λ_{node} to shorter wavelength is because the air cavity length decreased. The changes of the node wavelength ($\Delta\lambda_{node}$) produced by displacement δ were tracked and then adjusted by a linear fit. The adjusted curves for the three E-HFFPI$_{MCF}$s evaluated for displacement size of 0.1 μm are plotted in Fig. 8. The sensitivity of E-HFFPI$_{MCF1,2,3}$ was estimated at −42.3658, −29.3145, and −18.1204 nm/μm, respectively. It can be appreciated that the E-HFFPI$_{MCF1}$ with the large FSR, with ρ equal to 36.6 mm, exhibited the highest sensitivity. The E-HFFPI$_{MCF1}$'s resolution was calculated to be equal to 0.47 nm, this by considering that the FBG interrogator resolution was 20 pm, while the resolution of the E-HFFPI$_{MCF2}$ and E-HFFPI$_{MCF3}$ was estimated at around 0.68 nm and 1.10 nm. Such resolutions are almost twofold higher than those obtained with the first harmonic of the Vernier effect in Ref. [31].

The interference patterns shown in Fig. 6(b)–(d), of each E-HFFPI$_{MCF}$ have a large number of fringes. If the wavelength span of the spectrum is reduced to a narrow region, in order to observe a single dip at a wavelength denoted as λ_{FPI}. By tracking λ_{FPI} displacements, a demodulation method commonly used to assess the performance of the FPI sensors, it provides information about the sensibility of the E-HFFPI using the traditional analysis. Thus, the spectra obtained with the E-HFFPI$_{MCF1}$ were analyzed by tracking λ_{FPI}, where the peak is blue-shifted for each measured displacement of 0.1 μm, as shown in Fig. 9. The λ_{FPI} shift and the measured displacements are plotted and adjusted to a linear fit in the inset of Fig. 9. The estimated sensitivity and resolution of the E-HFFPI$_{MCF1}$, by considering a 20 pm resolution of the FBG interrogator, were found to be −0.54 nm/μm and 37 nm, respectively. The sensitivity of the E-HFFPI$_{MCF}$s is almost 80 times higher when the envelope analysis is used. It is important mentioning that the discrepancy in the sensitivities of the E-HFFPI$_{SMF}$ and the E-HFFPI$_{MCF}$, when the L_{air} has an ρ equal to 36.6 μm, can be due to the reference spectra that were taken.

4. Conclusions

In conclusion, an extrinsic hybrid fiber Fabry-Perot interferometer for nano-displacement sensing was proposed and demonstrated. The proposed technique allows to set up various E-HFFPI by using either an SMF or a supermode interferometer as a lead-in/out fiber tip and a mirrored microscope glass slide. In the E-HFFPI, a supermode interferometer may be used to measure long-range and non-contact nano-displacements. The hybrid structure is composed of two macro-cavities with different media. In our case, air and glass were used, but it is feasible to use liquids. The air and glass cavities are simple and easy to implement and do not require of micromachining processes that involve costly and tedious procedures. Various E-HFFPI with different characteristics were evaluated, the displacement resolution was found to be between 0.47 and 1.1 nm.

The concepts and approach reported here can be used for other applications. For example, it is feasible to monitor sub-nanometric dimension changes in materials caused by temperature, pressure, or by exposure to gases. Hence, the applications of our hybrid interferometer can be extended beyond displacements and can go up to chemical sensing or characterization of properties of materials.

Funding

Consejo Nacional de Ciencia y Tecnología (Mexico) through the Ph. D. scholarship of Monserrat del Carmen Alonso Murias and the Instituto de innovación, ciencia y emprendimiento para la competitividad del estado de Guanajuato (México) through the Project CIN006. This work is part of the project No. PGC2018-101997-B-I00, MCIN/AEI/10.13039/501100011033 and FEDER, *Una manera de hacer Europa*.

CRediT authorship contribution statement

Monserrat Alonso-Murias: Methodology, Formal analysis, Investigation, Writing – original draft, Visualization, Software. **David Monzón-Hernández:** Conceptualization, Methodology, Formal analysis, Writing – original draft, Validation, Visualization, Software. **Enrique Antonio-Lopez:** Conceptualization, Writing – review & editing, Resources. **Axel Schülzgen:** Conceptualization, Writing – review & editing, Resources. **Rodrigo Amezcua-Correa:** Conceptualization, Writing – review & editing, Resources. **Joel Villatoro:** Writing – review & editing, Resources, Funding acquisition.

Declaration of Competing Interest

The authors declare that they have no known competing financial interests or personal relationships that could have appeared to influence the work reported in this paper.

References

[1] W. Gao, Precision Nanometrology, first ed., Springer, London, London, 2010. <https://doi.org/10.1007/978-1-84996-254-4>.

[2] T. Taimre, M. Nikolić, K. Bertling, Y.L. Lim, T. Bosch, A.D. Rakić, Laser feedback interferometry: a tutorial on the self-mixing effect for coherent sensing, Adv. Opt. Photon. 7 (2015) 570, https://doi.org/10.1364/aop.7.000570.
[3] C.-C. Wu, Y.-Z. Chen, C.-H. Liao, Common-path laser planar encoder, Opt. Exp. 21 (2013) 18872, https://doi.org/10.1364/oe.21.018872.
[4] S. Zhao, C. Hou, J. Bai, G. Yang, F. Tian, Nanometer-scale displacement sensor based on phase-sensitive diffraction grating, Appl. Opt. 50 (2011) 1413–1416, https://doi.org/10.1364/AO.50.001413.
[5] D.T. Smith, J.R. Pratt, L.P. Howard, A fiber-optic interferometer with subpicometer resolution for dc and low-frequency displacement measurement, Rev. Sci. Instrum. 80 (2009), https://doi.org/10.1063/1.3097187.
[6] C. Guo, Y. Zhang, M. Klegseth, J. Gao, G. Chen, Micrometer-accuracy 2D displacement interferometer with plasmonic metasurface resonators, Opt. Lett. 45 (2020) 6474, https://doi.org/10.1364/OL.412130.
[7] X. Qi, S. Wang, J. Jiang, K. Liu, X. Wang, Y. Yang, T. Liu, Fiber optic fabry-perot pressure sensor with embedded mems micro-cavity for ultra-high pressure detection, J. Lightwave Technol. 37 (2019) 2719–2725, https://doi.org/10.1109/JLT.2018.2876717.
[8] J. Eom, C.J. Park, B.H. Lee, J.H. Lee, I.B. Kwon, E. Chung, Fiber optic Fabry-Perot pressure sensor based on lensed fiber and polymeric diaphragm, Sens. Actuat., A 225 (2015) 25–32, https://doi.org/10.1016/j.sna.2015.01.023.
[9] C.J. Easley, L.A. Legendre, M.G. Roper, T.A. Wavering, J.P. Ferrance, J.P. Landers, Extrinsic Fabry-Perot interferometry for noncontact temperature control of nanoliter-volume enzymatic reactions in glass microchips, Anal. Chem. 77 (2005) 1038–1045, https://doi.org/10.1021/ac048693f.
[10] Y. Huang, T. Wei, Z. Zhou, Y. Zhang, G. Chen, H. Xiao, An extrinsic Fabry-Perot interferometer-based large strain sensor with high resolution, Meas. Sci. Technol. 21 (2010), https://doi.org/10.1088/0957-0233/21/10/105308.
[11] S. Binu, V.P. Mahadevan Pillai, N. Chandrasekaran, Fibre optic displacement sensor for the measurement of amplitude and frequency of vibration, Opt. Laser Technol. 39 (2007) 1537–1543, https://doi.org/10.1016/j.optlastec.2006.12.008.
[12] T.K. Gangopadhyay, Non-contact vibration measurement based on an extrinsic Fabry-Perot interferometer implemented using arrays of single-mode fibres, Meas. Sci. Technol. 15 (2004) 911–917, https://doi.org/10.1088/0957-0233/15/5/019.
[13] E. Kendir, Ş. Yaltkaya, Variations of magnetic field measurement with an extrinsic Fabry-Perot interferometer by double-beam technique, Meas.: J. Int. Meas. Confed. 151 (2020) 107217, https://doi.org/10.1016/j.measurement.2019.107217.
[14] P. Chawah, R. Briand, V. Dupe, F. Boudin, M. Cattoen, F. Lizion, H.C. Seat, Direct non-invasive measuring techniques of nanometric liquid level variations using extrinsic fiber fabry-perot interferometers, IEEE Sens. J. 21 (2021) 1580–1587, https://doi.org/10.1109/JSEN.2020.3020512.
[15] J.N. Dash, R. Jha, J. Villatoro, S. Dass, Nano-displacement sensor based on photonic crystal fiber modal interferometer, Opt. Lett. 40 (2015) 467, https://doi.org/10.1364/ol.40.000467.
[16] K. Tian, J. Yu, X. Wang, H. Zhao, D. Liu, E. Lewis, G. Farrell, P. Wang, Miniature Fabry-Perot interferometer based on a movable microsphere reflector, Opt. Lett. 45 (2020) 787, https://doi.org/10.1364/ol.385222.
[17] R. Gao, D.F. Lu, J. Cheng, Y. Jiang, L. Jiang, Z.M. Qi, Optical displacement sensor in a capillary covered hollow core fiber based on anti-resonant reflecting guidance, IEEE J. Sel. Top. Quant. Electron. 23 (2017) 193–198, https://doi.org/10.1109/JSTQE.2016.2544705.
[18] C.J. Moreno-Hernandez, D. Monzon-Hernandez, A. Martinez-Rios, D. Moreno-Hernandez, J. Villatoro, Long-range interferometric displacement sensing with tapered optical fiber tips, IEEE Photon. Technol. Lett. 27 (2015) 379–382, https://doi.org/10.1109/LPT.2014.2375651.
[19] A.D. Gomes, H. Bartelt, O. Frazão, Optical vernier effect: recent advances and developments, Laser Photon. Rev. 15 (2021), https://doi.org/10.1002/lpor.202000588.
[20] Y. Ying, C. Zhao, H. Gong, S. Shang, L. Hou, Demodulation method of Fabry-Perot sensor by cascading a traditional Mach-Zehnder interferometer, Opt. Laser Technol. 118 (2019) 126–131, https://doi.org/10.1016/j.optlastec.2019.04.043.
[21] T. Paixão, F. Araújo, P. Antunes, Highly sensitive fiber optic temperature and strain sensor based on an intrinsic Fabry-Perot interferometer fabricated by a femtosecond laser, Opt. Lett. 44 (2019) 4833, https://doi.org/10.1364/ol.44.004833.
[22] J. Deng, D.N. Wang, Ultra-sensitive strain sensor based on femtosecond laser inscribed in-fiber reflection mirrors and vernier effect, J. Lightwave Technol. 37 (2019) 4935–4939, https://doi.org/10.1109/JLT.2019.2926066.
[23] F. Li, X. Li, X. Zhou, P. Gong, Y. Zhang, Y. Zhao, L.V. Nguyen, H. Ebendorff-Heidepriem, S.C. Warren-Smith, Plug-in label-free optical fiber DNA hybridization sensor based on C-type fiber Vernier effect, Sens. Actuat., B (2021) 131212, https://doi.org/10.1016/j.snb.2021.131212.
[24] A.D. Gomes, M.S. Ferreira, J. Bierlich, J. Kobelke, M. Rothhardt, H. Bartelt, O. Frazão, Hollow microsphere combined with optical harmonic Vernier effect for strain and temperature discrimination, Opt. Laser Technol. 127 (2020) 106198, https://doi.org/10.1016/j.optlastec.2020.106198.
[25] L.G. Abbas, Vernier effect-based strain sensor with cascaded fabry-perot interferometers, IEEE Sens. J. 20 (2020) 9196–9201, https://doi.org/10.1109/JSEN.2020.2988469.
[26] S. Zhang, L. Yin, Y. Zhao, A. Zhou, L. Yuan, Bending sensor with parallel fiber Michelson interferometers based on Vernier-like effect, Opt. Laser Technol. 120 (2019) 105679, https://doi.org/10.1016/j.optlastec.2019.105679.
[27] T. Nan, B. Liu, Y. Wu, J. Wang, Y. Mao, L. Zhao, T. Sun, J. Wang, Ultrasensitive strain sensor based on Vernier- effect improved parallel structured fiber-optic Fabry-Perot interferometer, Opt. Exp. 27 (2019) 17239, https://doi.org/10.1364/oe.27.017239.
[28] Z. Han, G. Xin, P. Nan, J. Liu, J. Zhu, H. Yang, Hypersensitive high-temperature gas pressure sensor with Vernier effect by two parallel Fabry-Perot interferometers, Optik (Stuttg). 241 (2021), https://doi.org/10.1016/j.ijleo.2021.166956.
[29] P. Robalinho, O. Frazão, Giant displacement sensitivity using push-pull method in interferometry, Photonics 8 (2021) 23, https://doi.org/10.3390/photonics8010023.
[30] Y. Yang, X. Zhang, L. Yang, Y. Yu, Z. Wang, T. Wang, Ultrahigh-sensitivity displacement sensing enabled by the Vernier effect with inhibited antiresonance, Opt. Lett. 46 (2021) 1053, https://doi.org/10.1364/ol.419203.
[31] P. Robalinho, O. Frazao, Nano-displacement measurement using an optical drop-shaped structure, IEEE Photon. Technol. Lett. 33 (2021) 65–68, https://doi.org/10.1109/LPT.2020.3044118.
[32] J.A. Flores-Bravo, R. Fernandez, J.E. Antonio-Lopez, J. Zubia, A. Schulzgen, R. Amezcua Correa, J. Villatoro, Simultaneous sensing of refractive index and temperature with a supermode interferometer, J. Lightwave Technol. (2021), https://doi.org/10.1109/JLT.2021.3113863.
[33] N. Cuando-Espitia, M.A. Fuentes-Fuentes, D.A. May-Arrioja, I. Hernandez-Romano, R. Martinez-Manuel, M. Torres-Cisneros, Dual-Point Refractive Index Measurements Using Coupled Seven-Core Fibers, Journal of Lightwave Technology 39 (2021) 310–319, https://doi.org/10.1109/JLT.2020.3022885.
[34] J. Villatoro, O. Arrizabalaga, G. Durana, I. Saéz De Ocáriz, E. Antonio-Lopez, J. Zubia, A. Schülzgen, R. Amezcua-Correa, Accurate strain sensing based on super-mode interference in strongly coupled multi-core optical fibres, Sci. Rep. 7 (2017) 1–7, https://doi.org/10.1038/s41598-017-04902-3.
[35] G. Salceda-Delgado, A. van Newkirk, J.E. Antonio-Lopez, A. Martinez-Rios, A. Schülzgen, R. Amezcua Correa, Compact fiber-optic curvature sensor based on super-mode interference in a seven-core fiber, Opt. Lett. 40 (2015) 1468, https://doi.org/10.1364/ol.40.001468.
[36] J. Villatoro, E. Antonio-Lopez, J. Zubia, A. Schülzgen, R. Amezcua-Correa, Interferometer based on strongly coupled multi-core optical fiber for accurate vibration sensing, Opt. Exp. 25 (2017) 25734, https://doi.org/10.1364/oe.25.025734.
[37] M.C. Alonso-Murias, D. Monzón-Hernández, O. Rodríguez-Quiroz, J.E. Antonio-Lopez, A. Schülzgen, R. Amezcua-Correa, J. Villatoro, Long-range multicore optical fiber displacement sensor, Opt. Lett. 46 (2021) 2224, https://doi.org/10.1364/ol.421004.
[38] L. Liu, T. Ning, J. Zheng, L. Pei, J. Li, J. Cao, X. Gao, C. Zhang, High-sensitivity strain sensor implemented by hybrid cascaded interferometers and the Vernier-effect, Opt. LASER Technol. 119 (2019), https://doi.org/10.1016/j.optlastec.2019.105591.
[39] O. Rodríguez-Quiroz, C.E. Domínguez-Flores, D. Monzón-Hernández, C. Moreno-Hernández, Hybrid fiber fabry-perot interferometer with improved refractometric response, J. Lightwave Technol. 37 (2019) 4268–4274, https://doi.org/10.1109/JLT.2019.2922836.